Ocean Engineering 293 (2024) 116627

Contents lists available at ScienceDirect

Ocean Engineering

journal homepage: www.elsevier.com/locate/oceaneng

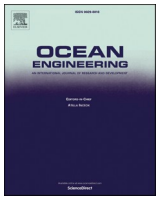

Research paper

Time-optimal control of ship manoeuvring under wave loads

Ming Zhang [a], Daejeong Kim [b,*], Tahsin Tezdogan [c], Zhi-Ming Yuan [a]

[a] Department of Naval Architecture, Ocean and Marine Engineering, University of Strathclyde, Glasgow, UK
[b] Division of Navigation Convergence Studies, Korea Maritime & Ocean University, Busan, South Korea
[c] Maritime Engineering, University of Southampton, Southampton, UK

ARTICLE INFO

Handling Editor: Prof. A.I. Incecik

Keywords:
Model predictive control
Path planning
Time-optimal manoeuvring
Trajectory tracking
Wave load

ABSTRACT

Ship manoeuvrability of Maritime Autonomous Surface Ships (MASS) revolutionise the maritime industry. However, this paradigm shift necessitates the advancement of manoeuvring control models to meet the complex demands of autonomous navigation. This paper addresses the need for an improved manoeuvring control model for MASS, particularly concerning path planning and tracking in the presence of wave loads. The paper establishes a comprehensive mathematical model for ship manoeuvring, considering forces acting on the ship's hull, propellers, rudders, and wave loads. A time optimisation model using a spatial reformulation approach is introduced. A nonlinear Model Predictive Control (MPC) model is presented for path planning and tracking, with a case study investigating the influence of wave load and comparing two control strategies. 10%–20% of time consumption increases if the wave load exists. This research bridges the gap in existing literature by incorporating wave loads into MPC-based control models for MASS. The findings shed light on the significance of wave loads in ship manoeuvring and provide valuable insights into effective control strategies for autonomous vessels operating in real-world sea conditions.

1. Introduction

The study of ship manoeuvrability has long been a central focus within the field of naval architecture and the shipping industry. However, with the rapid advancements in remote control, communication systems, observation technologies, and artificial intelligence, the concept of Maritime Autonomous Surface Ships (MASS) has emerged as a highly promising solution for enhancing the economic, efficient, and environmentally sustainable aspects of the shipping trade. Additionally, these autonomous vessels have demonstrated potential in offshore renewable energy transportation, as noted by Zhang et al. (2023b).

In light of these technological advancements and evolving maritime needs, there is a growing imperative to enhance the maneovuring control models for MASS. This necessity arises from the inherent complexities of autonomous navigation and the desire to bulid upon the conventional model introduced by Fossen (2011). Consequently, this paper aims to address the need for improved maneouvring control model for MASS in order to meet the evolving demands and opportunities within the maritime industry.

Designing a time-efficient path and trajectory represents one of the most formidable challenges in the realm of autonomous ship control. To achieve the minimum berthing time, a PID controller was employed, which involved solving nonlinear two-point boundary value problems (TPBVP) through a sequential conjugate gradient-restoration (SCGR) method (Ohtsu et al., 1996). Subsequently, path tracking was executed using a Proportional-Derivative (PD) controller, although it lacked anti-disturbance capabilities. Comparable methods were also explored in studies like (Okazaki and Ohtsu, 2008; Im, 2012). Given its inherently feedback-based nature, the PID controller exhibited limited efficacy in time optimisation scenarios. Mizuno et al. (2004) introduced an ANN-based Non-linear Model Predictive Control (NMPC) to compensate for control errors within ship manoeuvring simulations. Furthermore, Model Predictive Control (MPC) has been applied as an advanced controller for generating optimal control solutions. However, this approach relied on two separate control algorithms for the planning and tracking phases. Zhang et al. (2017) pioneered a robust model predictive control approach for path-following control in surface vessels, specifically to mitigate the effects of measurement noise. Wang et al. (2020) successfully achieved obstacle avoidance and path optimisation for autonomous underwater vehicles (AUVs) through an integration method that combines the MPC method, sliding mode control, and particle swarm optimisation. Recent years have witnessed substantial

* Corresponding author.
E-mail address: kdj4907@kmou.ac.kr (D. Kim).

https://doi.org/10.1016/j.oceaneng.2023.116627
Received 1 December 2023; Received in revised form 17 December 2023; Accepted 19 December 2023
Available online 5 January 2024
0029-8018/© 2023 The Author(s). Published by Elsevier Ltd. This is an open access article under the CC BY license (http://creativecommons.org/licenses/by/4.0/).

contributions from researchers in the field of path planning and tracking for surface ships, as evident in works such as (Oh and Sun, 2010; Wahl and Gilles, 1998; Helling et al., 2021; Pavlov et al., 2009; Huang et al., 2020).

It should be highlighted that ships are constantly exposed to environmental loads at actual sea conditions, which wave loads being the most significant factor affecting a ship's manoeuvring performance. Liu et al. (2017) developed a novel guidance and control system for USVs in consideration of environmental influences. A robust autopilot module and an intelligent path planning module were integrated into their system. Kim et al. (2017) proposed a path optimisation method based on a genetic algorithm and a new fitness function. Environmental loads and travel time were considered in their study. Huang et al. (2019) proposed a trajectory tracking controller for USVs with multiple uncertainties and input constraints. In their study, a trajectory tracking guidance law based on yaw angle and surge motion was used. The inner and outer disturbances were observed by reduced order extended state observers in their controller.

It should be noted that there have been numerous studies utilising MPC controllers to generate optimal control results for MASS in calm waters. However, calm water conditions do not accurately represent the real operating conditions of autonomous ships at sea. To the best of the authors' knowledge, there appears to be a deficiency in research that takes into account external loads affecting a ship's manoeuvrability when generating optimal control results using MPC methods. For example, a MPC-based control strategy was developed for autonomous ship path planning and tracking in (Zhang et al., 2022, 2023a). However, as a key influence of ship manoeuvring, wave load is not considered. This paper will introduce wave load in the MPC-based control model to refine the mathematical model and extend two control strategies under wave load. There are two questions will be answered in this study:

1. What is the impact of wave load to path planning and tracking of the ship manoeuvring?
2. Which type of control strategies is better for ship manoeuvring under wave loads?

In Section 2, the mathematical model of ship manoeuvring will be established. The forces acting on ship's hulls, propellers rudders and wave load are treated separately. A time optimisation model by a spatial reformulation approach will be introduced in section 3. In Section 4, a nonlinear MPC model is introduced for path planning and tracking of the ship manoeuvring. A case study of ship manoeuvring control, including time-optimal path planning and tracking, will be investigated to analyse the impact of wave load and evaluate two control strategies in Section 5, followed by conclusions in Section 6.

2. Mathematical model of ship manoeuvring

In this section, mathematical model of ship manoeuvring illustrates the hydrodynamic of a ship. The forces acting on the ship are expressed. In the article, superscript prime (') represents derivate with respect to space; superscript dot ($\dot{\cdot}$) represents derivate with respect to time; superscript (^{dl}) represents dimensionless value.

When designing course autopilots, it is often convenient to normalise the ship steering equations of motion with respect to the vessel speed, U. Dimensionless hydrodynamic derivatives are derived based on the Froude criterion in this study. Dimensionless variables are derived by the prime system II of SNAME (Fossen, 2011). The limitation of the dimensionless system is that the time under the zero-speed state cannot be expressed. Thus, the numerical simulation will not discuss the zero-speed condition.

Table 1 shows the variables and dimension used for the prime system II. The Length, L, is the ship length between perpendiculars (L_{pp}). The limitation of the dimensionless system is that the time under the zero-speed state cannot be expressed. Thus, the numerical simulation will not discuss the zero-speed condition.

Table 1
Dimensionless variables used for the prime systems II.

Variable	Dimension
Length	L
Mass	$1/2\rho L^2 D$
Inertia moment	$1/2\rho L^4 D$
Time	L/U
Reference area	LD
Position	L
Angle	1
Linear velocity	U
Angular velocity	U/L
Linear acceleration	U^2/L
Angular acceleration	U^2/L^2
Force	$1/2\rho U^2 LD$
Moment	$1/2\rho U^2 L^2 D$

2.1. Assumptions and limitations

The following assumptions (Yasukawa and Yoshimura, 2015) are deployed as follows,

- Ship is a rigid body.
- Hydrodynamic forces acting on the ship are treated quasi-steadily.
- Lateral velocity component is small compared with longitudinal velocity component.
- Ship speed is not fast that wave-making effect can be neglected.
- Metacentric height GM is sufficiently large, and the roll couple effect on manoeuvring is negligible.
- Manoeuvring motions are affected by the low-frequency wave responses.

There are limitations of the proposed study regarding to the assumptions: the proposed ship manoeuvring model is incapable to describe high-speed ship manoeuvring. Mean drift wave loads are considered while periodical dynamic wave load is neglected. Conventional propeller and rudder are adopted, and regular wave are discussed.

2.2. Coordinate systems

Only 3-Degree-of-Freedom (3-DoF) motions in the horizonal plane (surge, sway, and yaw) will be considered in this article because the motions of the other DoFs (roll, pitch and heave) have insignificant impact to the manoeuvring operation. Fig. 1 shows the coordinate systems used in the ship manoeuvring mathematical model: the earth-fixed coordinate system, o_0-x_0y_0, where x_0-y_0 plane coincides with the still water surface, and the moving ship-fixed coordinate system, o-xy, where o is taken on the midship of the vessel, and x and y point towards the ship's bow and the starboard, respectively. u and v_m denote the velocity components in x and y directions at the midship position, respectively; r is the yaw rate; Heading angle, ψ, is defined as the angle between x_0 and x axes; drift angle at the midship position, $\beta = \tan^{-1}(-v_m/u)$; the resultant velocity, $U = \sqrt{u^2 + v_m^2}$. δ is the rudder angle; U_R is the resultant inflow velocity of the rudder; u and v_m denote the inflow velocity components of the rudder in x and y directions, respectively; F_N is the rudder normal force; α_R is the attack angle of rudder.

The present model utilizes a coordinate system fixed to the midship position which is convenient for simulation with different loading conditions. Employing the midship-based coordinate system can avoid position change of the center of gravity (Yasukawa and Yoshimura, 2015).

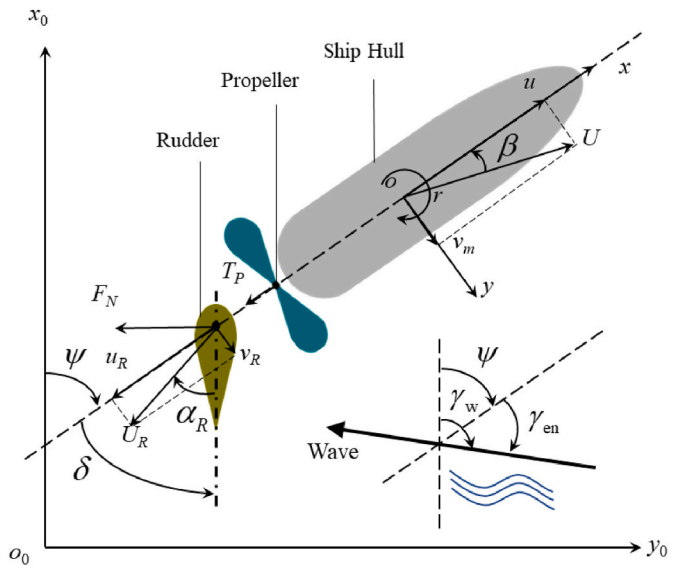

Fig. 1. 3-DoF Coordinate systems of ship manoeuvring mathematical model.

2.3. Motion equations

The mathematical model of the manoeuvring motion is established on the body-fixed coordinate frame. Transformation matrices are required to bridge the trajectories of ship under the two coordinate frames. Displacement transformation is expressed as follows:

$$\begin{bmatrix} x_0 \\ y_0 \end{bmatrix} = \begin{bmatrix} \cos\psi & -\sin\psi \\ \sin\psi & \cos\psi \end{bmatrix} \begin{bmatrix} x \\ y \end{bmatrix} + \begin{bmatrix} x_m \\ y_m \end{bmatrix}, \tag{1}$$

where (x_0, y_0) is the current position of the midship in the earth-fixed coordinate o_0-x_0y_0; (x, y) is the current position of the midship in the ship-fixed coordinate; (x_m, y_m) is the initial position of the midship in the earth-fixed coordinate o_0-x_0y_0. Moreover, the following velocity transformation equation is the derivative of Equation (1):

$$\begin{bmatrix} \dot{x}_0 \\ \dot{y}_0 \\ \dot{\psi} \end{bmatrix} = \begin{bmatrix} \cos\psi & -\sin\psi & 0 \\ \sin\psi & \cos\psi & 0 \\ 0 & 0 & 1 \end{bmatrix} \begin{bmatrix} u \\ v \\ r \end{bmatrix}, \tag{2}$$

where yaw motion in the horizontal plane is added in Equation (2).

In the control system of ship manoeuvring, the propeller rotation speed and rudder angle are treated as manipulated variables (MVs). Displacements and velocities are referred to as states variables. In the present model, six states and two MVs are used to simulate the manoeuvring operation which are expressed as follows:

$$\begin{aligned} X_t &= [x_0 \quad y_0 \quad \psi \quad u \quad v \quad r]^{\mathrm{T}} \\ u_t &= [n_p \quad \delta]^T \end{aligned}, \tag{3}$$

where X_t is the state vector and u_t is the MV vector in the temporal coordinate. The former three variables in the state vector are displacements in the earth-fixed coordinate system and the latter three variables are the velocity components in the body-fixed coordinate system. The variables in the MV vector include the propeller rotation speed n_p and the rudder angle δ.

The manoeuvring equations are represented in surge, sway and yaw directions as follows:

$$\begin{aligned} m\dot{u} - mvr &= F_X \\ m\dot{v} + mur &= F_Y \\ I_{zG}\dot{r} &= N \end{aligned}, \tag{4}$$

where m is the mass of ship; I_{zG} is the moment of inertia of ship around center of gravity. F_x, F_y and N are the external forces in surge, sway, and yaw directions respectively which are represented as follows:

$$\begin{aligned} F_x &= -m_x\dot{u} + m_y v_m r + X_m \\ F_y &= -m_y\dot{v}_m + m_x ur + Y_m \\ N &= -J_z\dot{r} + N_m - x_G F_y \end{aligned}, \tag{5}$$

where F_x and F_y are the surge force and sway force acting on ship; N is the yaw moment acting on ship around center of gravity; m_x and m_y are the added masses of the x axis direction and y axis direction, respectively; J_z is the added moment of inertia. The center of gravity of ship is located at $(x_G, 0, 0)$ in o–xyz system. x_G is the longitudinal coordinate of the center of gravity of ship. X_m, Y_m and N_m are surge force, sway force, yaw moment around midship except added mass components, respectively. The sway velocity component at the center of gravity (CoG), v is expressed as follows,

$$v = v_m + x_G \cdot r. \tag{6}$$

Substituting Equations (5) and (6) into Equation (4) for eliminating v,

$$\begin{aligned} &(m + m_x)\dot{u} - (m + m_y)v_m r - x_G m r^2 = X_m \\ &(m + m_y)\dot{v}_m + (m + m_x)ur + x_G m\dot{r} = Y_m \\ &(I_{zG} + x_G^2 m + J_z)\dot{r} + x_G m(\dot{v}_m + ur) = N_m \end{aligned}. \tag{7}$$

Equation (7) is the motion equation to be solved of which unknown variables are u, v_m and r. The external force in the right-hand side of Equation (7) consists of four components, the ship hull hydrodynamic force, the propeller force, the rudder force and the wave force, which are expressed as

$$\begin{aligned} X_m &= X_{\mathrm{H}} + X_{\mathrm{P}} + X_{\mathrm{R}} + X_{\mathrm{W}} \\ Y_m &= Y_{\mathrm{H}} + Y_{\mathrm{P}} + Y_{\mathrm{R}} + Y_{\mathrm{W}} \\ N_m &= N_{\mathrm{H}} + N_{\mathrm{P}} + N_{\mathrm{R}} + N_{\mathrm{W}} \end{aligned}, \tag{8}$$

where the subscripts H, P, R and W represent the ship hull, propeller, rudder and wave, respectively.

2.4. Hydrodynamic forces acting on a ship hull

X_{H}, Y_{H} and N_{H} are expressed as follows:

$$\begin{aligned} X_{\mathrm{H}} &= -R_0 + X_{vv}v_m^2 + X_{vr}v_m r + X_{rr}r^2 + X_{vvvv}v_m^4 \\ Y_{\mathrm{H}} &= Y_v v_m + Y_r r + Y_{vvv}v_m^3 + Y_{vvr}v_m^2 r + Y_{vrr}vr^2 + Y_{rrr}r^3 \\ N_{\mathrm{H}} &= N_v v_m + N_r r + N_{vvv}v_m^3 + N_{vvr}v_m^2 r + N_{vrr}v_m r^2 + N_{rrr}r^3 \end{aligned}, \tag{9}$$

where X_{vv}, X_{vr}, X_{rr}, X_{vvvv}, Y_v, Y_r, Y_{vvv}, Y_{vvr}, Y_{vrr}, Y_{rrr}, N_v, N_r, N_{vvv}, N_{vvr}, N_{vrr}, and N_{rrr} are called the hydrodynamic derivatives on maneuvering.

2.5. Hydrodynamic force due to propeller

Surge force due to propeller X_{P} is expressed as

$$\begin{aligned} X_{\mathrm{P}} &= (1 - t_{\mathrm{P}})T_{\mathrm{P}} \\ Y_{\mathrm{P}} &= 0 \\ N_{\mathrm{P}} &= 0 \end{aligned}, \tag{10}$$

where the thrust deduction factor t_{P} is assumed to be constant at a given propeller load for simplicity. The propeller forces in sway and yaw directions are excluded. Instead of this, the steering effect is taken into account at the rudder force component X_{R} as shown in the next subsection of rudder force. Propeller thrust T_{P} is written as

$$T_{\mathrm{P}} = \rho n_{\mathrm{P}}^2 D_{\mathrm{P}}^4 K_T(J_{\mathrm{P}}), \tag{11}$$

where K_T is approximately expressed as a 2nd polynomial function of propeller advanced ratio J_{P}:

$$K_T(J_{\mathrm{P}}) = k_0 + k_1 J_{\mathrm{P}} + k_2 J_{\mathrm{P}}^2. \tag{12}$$

J_{P} is written as

$$J_P = \frac{(1-w_P)u}{n_P D_P}. \tag{13}$$

The w_P changes with manoeuvring motion in general which is presented as (Yasukawa and Yoshimura, 2015)

$$(1-w_P)/(1-w_{P0}) = 1 + \{1 - \exp(-C_1|\beta_P|)\}(C_2 - 1), \tag{14}$$

where β_P is the geometrical inflow angle to the propeller in maneuvering motions, which is defined as

$$\beta_P = \beta - x_P r. \tag{15}$$

C_1 and C_2 in Equation (14) are constant coefficients.

2.6. Hydrodynamic force due to rudder

Effective rudder forces X_R, Y_R and N_R are expressed as (Maki et al., 2020)

$$\begin{aligned} X_R &= -(1-t_R)F_N \sin\delta \\ Y_R &= -(1+a_H)F_N \cos\delta \\ N_R &= -(x_R + a_H x_H)F_N \cos\delta \end{aligned}. \tag{16}$$

Note that the rudder tangential force is neglected in Equation (16). The t_R, a_H and x_H are the coefficients representing mainly hydrodynamic interaction between ship hull and rudder. The t_R is the steering resistance deduction factor and defined the deduction factor of rudder resistance versus $F_N \sin\delta$ (Matsumoto and Suemitsu, 1980). X_R includes a component of the propeller thrust change due to steering as mentioned in subsection 2.5. Therefore, t_R means a factor of both the rudder resistance deduction and the propeller thrust increase induced by steering. a_H and x_H are called the rudder force increase factor and the position of an additional lateral force component, respectively. The a_H represents the factor of lateral force acting on ship hull by steering versus $F_N \cos\delta$ which means the lateral component of F_N. The x_H means the longitudinal acting point of the additional lateral force component. The measured value of x_H is about $0.45L_{pp}$ which means the longitudinal acting point of the additional lateral force component. x_R is the longitudinal coordinate of rudder position which is of $-0.5L_{pp}$.

Rudder normal force, F_N, is expressed as

$$F_N = \begin{cases} \frac{1}{2}\rho A_R f_\alpha U_R^2 \sin\alpha_R & (n_p \geq 0) \\ 0 & (n_p < 0) \end{cases}, \tag{17}$$

where A_R is the rudder area. f_α is the rudder lift coefficient estimated by Fujii's formula (Fujii and Tuda, 1961) expressed as follows:

$$f_\alpha = \frac{6.13\Lambda}{2.25 + \Lambda} \tag{18}$$

where Λ is the aspect ratio of rudder surface. The resultant rudder inflow velocity U_R and the attack angle of rudder α_R are expressed as follows:

$$U_R = \sqrt{u_R^2 + v_R^2}, \tag{19}$$

$$\alpha_R = \delta - \tan^{-1}\left(\frac{v_R}{u_R}\right) \simeq \delta - \frac{v_R}{u_R}. \tag{20}$$

Assuming that the helm angle is zero when β and r are zeros, v_R can be expressed as

$$v_R = U\gamma_R \beta_R, \tag{21}$$

where γ_R is the flow straightening coefficient and

$$\beta_R = \beta - l_R r, \tag{22}$$

where l_R, which can be obtained from the captive model test, is treated as an experimental constant. The γ_R characteristic considerably affects the maneuvering simulation. Thus, γ_R should be captured correctly. Value of γ_R generally takes different magnitude for port and starboard turning (Fujii and Tuda, 1961).

The longitudinal inflow velocity component to rudder u_R is expressed as follows:

$$u_R = \varepsilon u(1-w_P)\sqrt{\eta\left\{1 + \kappa\left(\sqrt{1 + \frac{8K_T}{\pi J_P^2}} - 1\right)\right\}^2 + (1-\eta)}, \tag{23}$$

where means a ratio of wake fraction at rudder position to that at propeller position defined as

$$\varepsilon = (1-w_R)/(1-w_P). \tag{24}$$

In Eq. (23), κ is an experimental constant. w_R is the wake coefficient at rudder position. η is the ratio of propeller diameter to rudder span, namely, D_P/H_R.

2.7. Wave load acting on the ship hull

Uni-directional regular wave is considered in the present numerical simulation. Since the manoeuvring motions are mainly affected by the low-frequency wave responses, second order mean drift forces are calculated (Salvesen, 1974). The second order mean drift forces is dependent to encounter wave frequency ω_{en} and encounter wave heading angle γ_{en}. The waves satisfy the dispersion equation

$$\omega^2 = gk\tanh(kd), \tag{25}$$

where ω is the wave frequency, k is the wave number, and d is the wave depth. For deep water,

$$\omega^2 = gk. \tag{26}$$

The relationship between wave length λ and wave number k is shown as follows:

$$\lambda = \frac{2\pi}{k}. \tag{27}$$

The encounter wave frequency ω_{en} is

$$\omega en = \omega\left(1 - U\frac{\omega}{g}\cos\gamma en\right). \tag{28}$$

The encounter wave heading angle γ_{en}.

$$\gamma_{en} = \gamma_w - \psi, \tag{29}$$

where γ_w is the wave incident angle.

The wave length is not less than 0.5 L whose low-frequency citation is dominant. The longitudinal and lateral drift forces and the 2nd-order yaw moments are pre-calculated for a range of resultant speed U and encounter heading angle γ_{en} under a range of incident wave length. The wave forces acting on the ship hull are derived as follows:

$$\begin{aligned} X_W &= C_{WX}\rho g A_W^2 B^2/L \\ Y_W &= C_{WY}\rho g A_W^2 B^2/L \\ N_W &= C_{WN}\rho g A_W^2 B^2 \end{aligned}, \tag{30}$$

where C_{WX}, C_{WY} and C_{WN} are the hydrodynamic coefficients of wave induced forces and moment in surge, sway and yaw directions. A_W is the amplitude of the incident wave. The longitudinal, lateral drift forces and yaw moment are ranged of between 0° and 360°. B is the ship breadth.

3. Time optimisation model

The manoeuvring model introduced in Section 2 is the temporal hydrodynamic model, which cannot be directly used to derive the time optimal solution. Therefore, reparameterisation is required to make the time an optimisation variable. This study proposes a novel model

transformation to transform the temporal formulation to a spatial one. A curve variable is an independent variable. All states are dependent on the curve variable, including time. Time optimisation in temporal coordinate is realised approximately by numerical iteration. However, through the reformulation, the manoeuvring time is expressed clearly as a function mathematically which can be optimised in a theoretical approach.

3.1. Reference curve variable

The coordinate system adopted in the spatial reformulation of the ship manoeuvring model is shown in Fig. 2. (x_m, y_m) is the position of midship in the earth-fixed frame. There is a point on the curve whose radius of curvature, ρ^σ, just cross through the centroid of the vessel. ψ^σ is the heading angle in the spatial coordinate and $\dot{\psi}^\sigma$ is its derivative. u^σ is the component along the tangential direction of curvature. $\dot{s}$ is the projection of u^σ onto the tangential line. The red dot curve $\sigma(s)$ serves as a spatial coordinate, where s is an independent variable instead of the time t. If the position states X_0, Y_0 and ψ from the earth-fixed coordinate X_0-Y_0 are projected onto σ, they can be replaced by a new set of displacement states in the spatial coordinate.

$$\begin{aligned} e_y &= \cos(\psi^\sigma)(y_m - y^\sigma) - \sin(\psi^\sigma)(x_m - x^\sigma) \\ e_\psi &= \psi - \psi^\sigma \end{aligned}, \tag{31}$$

where e_y is the lateral deviation of the vessel to the reference curve, e_ψ is the rotational deviation to the reference tangential direction and X^σ , Y^σ and ψ^σ are the position states and rotational state of a reference point on the path given by the independent variable s. The manoeuvring deviation in temporal coordinate is transferred to the spatial one.

Assuming the vessel is not at rest at any time instant (i.e., $\dot{s} \neq 0$), the state vector can be expressed in the spatial coordinate. The extended state vector with the two new states can be written as follows:

$${}^cX_S = \left[x_0(s) y_0(s) \psi(s) u(s) v(s) r(s) e_y(s) e_\psi(s)\right]^T, \tag{32}$$

where e_y (s) and e_ψ (s) are the unique state variables which are meaningful only in a spatial coordinate.

3.2. Spatial reformulation

An extended state vector of Equation (3) in a temporal coordinate is required, which can be expressed as follows:

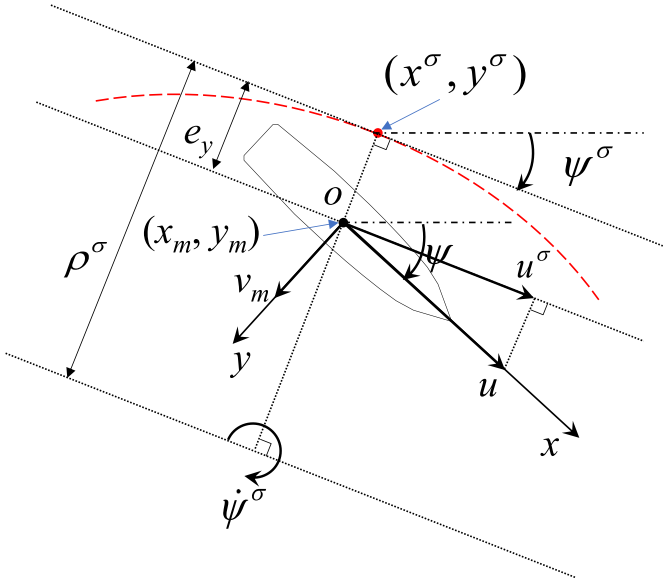

Fig. 2. Definition of the coordinate system in the reformulation coordinate.

$$X_{t,ext} = \left[X_t^{\mathrm{T}} \quad e_y(t) \quad e_\psi(t)\right]^{\mathrm{T}}, \tag{33}$$

where e_y (t) and e_ψ (t) do not have a physical meaning in a temporal coordinate. The definitions of e_y and e_ψ are based on the spatial curve s in the spatial coordinate. When the states are expressed in the temporal coordinate, the spatial curve does not exist. Therefore, the expressions of e_y and e_ψ can be calculated, however, the definitions are meaningless in the temporal coordinate. Introducing e_y and e_ψ is to establish an augmented matrix of the temporal model with the same size of the spatial model.

$$X_s' = \frac{dX_s'}{ds} = \frac{dX_s'}{dt}\frac{dt}{ds} = \frac{1}{\dot{s}}\dot{X}_{t,ext}, \tag{34}$$

where the superscript prime is used to represent the spatial derivative with respect to the curve and the superscript dot is used to represent the temporal derivative with respect to time. Velocity along the path is derived by the velocity with respect to the curve (Verschueren et al., 2014). The expression of $\dot{s}$ is by state variables based on the expression of surface derivative,

$$\dot{s} = \rho^\sigma \dot{\psi}^\sigma = \frac{\rho^\sigma}{\rho^\sigma - e_y}(u\cos(e_\psi) - v\sin(e_\psi)), \tag{35}$$

where ρ^σ is the radius of curvature of the reference path. The derivatives of the last two state variables in Equation (35) with respect to time are expressed as follows:

$$\begin{aligned} \dot{e}_y &= u\sin(e_\psi) + v\cos(e_\psi) \\ \dot{e}_\psi &= \dot{\psi} - \dot{\psi}^\sigma \end{aligned}. \tag{36}$$

With the reformulation of the manoeuvring model in a spatial coordinate, total time of manoeuvring operation T, which is the optimisation target, can be written as follows:

$$T = \int_{t_0}^{t_f} 1dt = \int_{s_0}^{s_f} tds = \int_{s_0}^{s_f} \frac{1}{\dot{s}} ds, \tag{37}$$

where the subscripts 0 and f indicate the start (lower bound) and end (upper bound), respectively, of the integration; dt is time increment in the temporal coordinate and d is the curve increment in the spatial coordinate.

3.3. Straight-line curve simplicity

Assuming the curve is a straight line, $\rho^\sigma \gg e_y$ and $\dot{\psi}^\sigma = 0$ as shown in

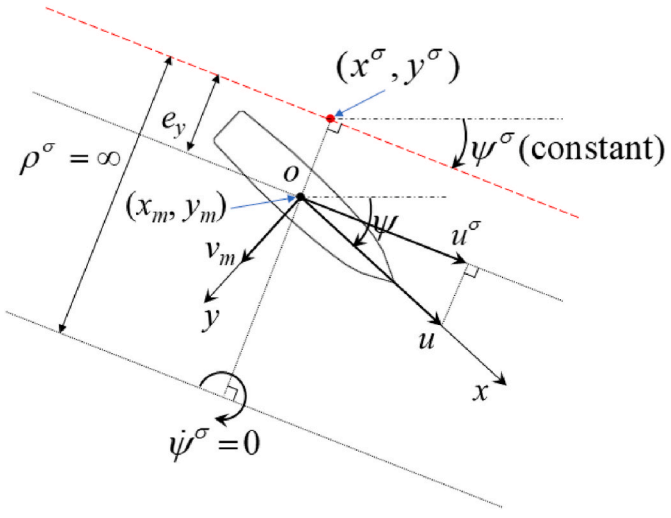

Fig. 3. Definition of the state variables in the straight-line coordinate system.

Fig. 3. Thereafter, the expression of the manoeuvring model in a spatial coordinate can be simplified as follows:

$$\begin{matrix} \dot{s} = u\cos(e_\psi) - v\sin(e_\psi) \\ \dot{e}_\psi = \dot{\psi} \end{matrix}. \tag{38}$$

Given that these variables are involved in the majority of the state representatives, such simplification will accelerate optimisation iteration in the numerical simulations. All manoeuvring operations in this study are based on the preceding hydrodynamic equations of the MMG model. With the given manoeuvring equation, a control system can be built and implemented.

4. Model predictive control strategy

4.1. MPC algorithm

This study will apply a nonlinear MPC to a ship manoeuvring problem owing to the nonlinear nature of the manoeuvring operation.

The open-loop control (receding horizon control) inside the MPC controller is shown in Fig. 4. The initial inputs are defined randomly. The input control the plant model and the MPC controller optimise the input based on cost function and constraints. The updated control inputs generate the updated outputs. The input and output are iteratively optimised in a prediction horizon. The plant model is a simplified estimation of actual plant which accelerates the optimisation process. The initial input of the control system is random in a certain prediction horizon and import to the plant model. The controller will optimise the control input based on the defined cost function. The MPC controller is designed with the support of MATLAB Model Predictive Controller Toolbox. The main modular of numerical model is user-defined, like cost function, state space and constraints. The unmentioned modular are set as default, such as dynamic optimiser (see Fig. 5).

4.2. State space representative

Given that states and MVs are coupled in a dynamic plant model, the state space of nonlinear MPC (Kouvaritakis and Cannon, 2016) is expressed as follows:

$$\begin{matrix} \dot{X}_t = f_t(X_t, u_t) \\ \dot{Y}_t = h_t(X_t, u_t) \end{matrix}. \tag{39}$$

In the nonlinear MPC Toolbox of Matlab, nonlinear MPC controllers solve nonlinear programming problems using the *fmincon* function with the sequential quadratic programming (SQP) algorithm, which requires Optimisation Toolbox software. The SQP algorithm requires linearised state space to generate the optimised control input in each prediction horizon.

The nonlinear model can be represented in a formation of linear time-invariant (LTI) state space representative as follows:

$$\begin{matrix} \dot{X}_t = A_t X_t + B_t u_t \\ Y_t = C_t X_t + D_t u_t \end{matrix}, \tag{40}$$

where Y_t is the observation matrix. The first row in Equation (40) is the description of the manoeuvring model. Observation Y_t is the same as state X_t when $C_t = \mathbf{I}$ and $D_t = \mathbf{0}$, where $\mathbf{I}$ is a unit matrix and $\mathbf{0}$ is a zero matrix.

The earth-fixed state variables are dependent on ψ, u, v and r. The body-fixed state variables are dependent on u, v, r and MVs. Define generalised mass matrix and generalised force matrix as follows:

$$M = \begin{bmatrix} m + m_x & 0 & 0 \\ 0 & m + m_y & x_G m \\ 0 & x_G m & I_{zG} + x_G^2 m + J_z \end{bmatrix} \tag{41}$$

$$F = \begin{bmatrix} X_m + (m + m_y) v_m r + x_G m r^2 \\ Y_m - (m + m_x) u r \\ N_m - x_G m u r \end{bmatrix} \tag{42}$$

The body-fixed state variables are derived as

$$\begin{bmatrix} \dot{u} \\ \dot{v} \\ \dot{r} \end{bmatrix} = M^{-1} F \tag{43}$$

Since not all the states are coupled, the expression and calculation of A_t and B_t in the Jacobian matrix are simplified as sparse matrices (Zhang et al., 2022).

4.3. Temporal-spatial transformation

Extended state vector in temporal coordinate is likewise expressed as follows:

$$\dot{X}_{t,\text{ext}} = A_{t,\text{ext}}^{8\times 8} X_{t,\text{ext}} + B_{t,\text{ext}}^{8\times 2} u_{t,\text{ext}}, \tag{44}$$

where $A_{t,\text{ext}}^{8\times 8}$ is an 8×8 extended Jacobian coefficient matrix of the state vectors and $B_{t,\text{ext}}^{8\times 2}$ is an 8×2 extended Jacobian coefficient matrix of MV vectors. The derivation of the extended state space representative in a temporal coordinate can be written as

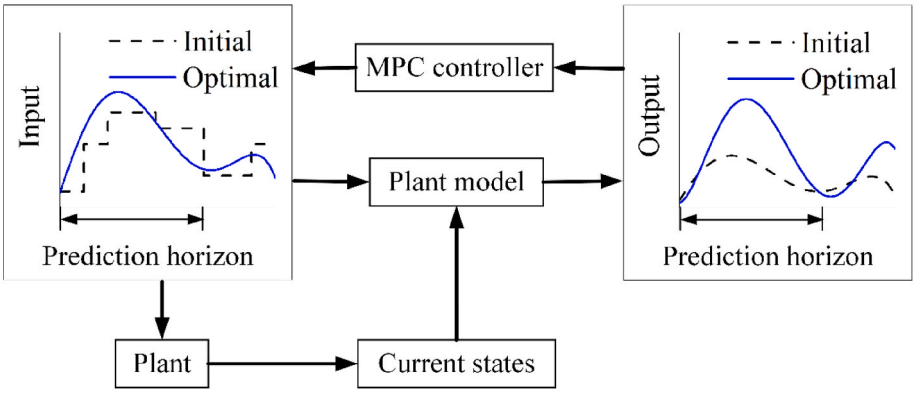

Fig. 4. Optimisation open loop of the MPC controller.

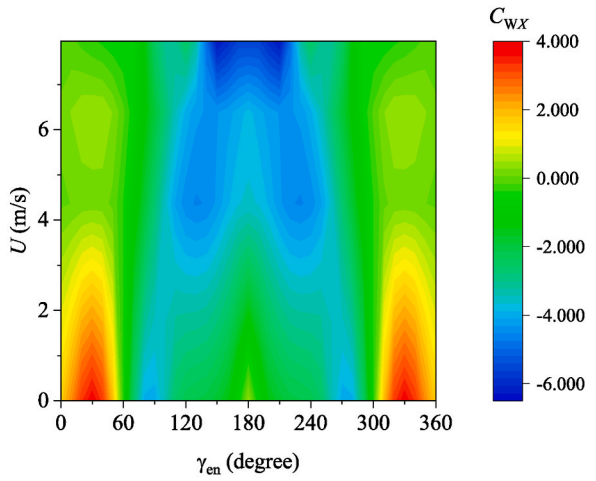

(a) Hydrodynamic coefficient of surge wave force, C_{WX}.

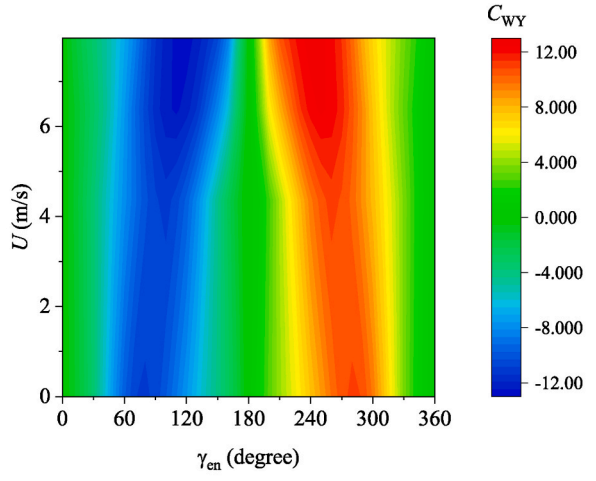

(b) Hydrodynamic coefficient of sway wave force, C_{WY}.

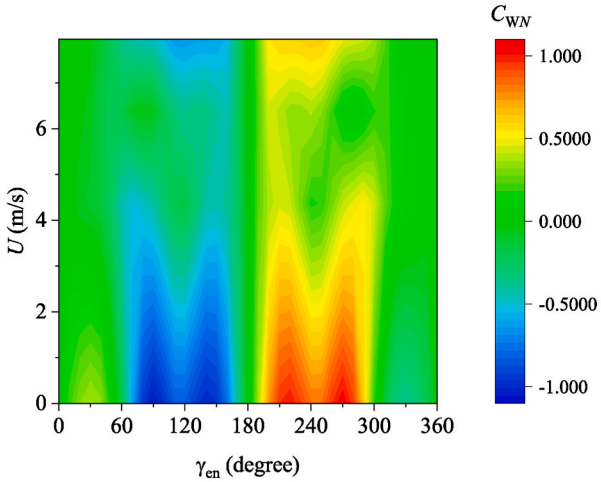

(c) Hydrodynamic coefficient of yaw wave moment, C_{WN}.

Fig. 5. Hydrodynamic coefficients of wave induced forces and moment (U = 0–7.96 m/s, γ_{en} = 0–360°, λ = 1.0 L).

$$A_{t,\mathrm{ext}}^{8\times8} = \frac{\partial \dot{X}_{t,\mathrm{ext}}}{\partial X_{t,\mathrm{ext}}} = \begin{bmatrix} \frac{\partial \dot{X}_t}{\partial X_t} & \frac{\partial \dot{X}_t}{\partial e_y} & \frac{\partial \dot{X}_t}{\partial e_\psi} \\ \frac{\partial \dot{e}_y}{\partial X_t} & \frac{\partial \dot{e}_y}{\partial e_y} & \frac{\partial \dot{e}_y}{\partial e_\psi} \\ \frac{\partial \dot{e}_\psi}{\partial X_t} & \frac{\partial \dot{e}_\psi}{\partial e_y} & \frac{\partial \dot{e}_\psi}{\partial e_\psi} \end{bmatrix}$$

$$B_{t,\mathrm{ext}}^{8\times2} = \frac{\partial \dot{X}_{t,\mathrm{ext}}}{\partial u_{t,\mathrm{ext}}} = \begin{bmatrix} \frac{\partial \dot{X}_t}{\partial u_t} & \frac{\partial \dot{X}_t}{\partial u_t} & \frac{\partial \dot{X}_t}{\partial u_t} \end{bmatrix} \tag{45}$$

According to Equations (31), (36) and (39), the state space in spatial coordinate can be expressed as

$$\begin{aligned} &\frac{\partial \dot{X}_t}{\partial X_t} = A_t \\ &\frac{\partial \dot{e}_y}{\partial X_t} = [0 \quad 0 \quad 0 \quad \sin(e_\psi) \quad \cos(e_\psi) \quad 0] \\ &\frac{\partial \dot{e}_\psi}{\partial X_t} = \frac{\partial \psi}{\partial X_t} - \frac{1}{\rho^\sigma} \\ &\frac{\partial \dot{e}_y}{\partial e_\psi} = u\cos(e_\psi) - v\sin(e_\psi) \\ &\frac{\partial \dot{X}_t}{\partial e_y} = \frac{\partial \dot{X}_t}{\partial e_\psi} = \frac{\partial \dot{e}_y}{\partial e_y} = \frac{\partial \dot{e}_\psi}{\partial e_y} = \frac{\partial \dot{e}_\psi}{\partial e_\psi} = 0 \end{aligned} \tag{46}$$

The state space representatives for the manoeuvring model in a spatial coordinate is

$$X' = A_s^{8\times8} X_s + B_s^{8\times2} u_s, \tag{47}$$

where X_s is the state vector, us is the MV vector, A_s is an 8 × 8 Jacobian coefficient matrix with respect to the state vectors. B_s is an 8 × 2 Jacobian coefficient matrix with respect to the MV vector, u_s is the control input in the temporal coordinate. All of these matrices are expressed in a spatial coordinate.

The Jacobian matrices, A_t and B_t, can be derived by using numerical method with MATLAB Deep Learning Toolbox (MathWorks, 2019).

4.4. Cost function and constraints

Expressions of cost function and constraints determine the optimisation process and optimal output values. The influence of states and MVs in the cost function are considered as follows:

$$\begin{aligned} \min J(X_t, u_t) &= \min \int_{t_0}^{t_f} L(X_t, u_t) dt \\ \min J(X_s, u_s) &= \min \int_{s_0}^{s_f} L(X_s, u_s) ds \end{aligned} \tag{48}$$

where J is the cost function, the subscripts t and s represent temporal and spatial coordinates, respectively. The functionality of the MPC controller is to minimise the cost function. Meanwhile, L is the target function.

$$\begin{aligned} \min J(X_t, u_t) &= \min \int_{t_0}^{t_f} L(X_t, u_t) dt \\ \min J(X_s, u_s) &= \min \int_{s_0}^{s_f} L(X_s, u_s) ds \end{aligned} \tag{49}$$

In the path planning stage, the cost function of nonlinear MPC controller is defined as time consumption of the berthing operation with constraints, which are varying ranges of state and MVs and varying ranges of their derivatives. Time consumption is expressed as a function of curve variable in spatial coordinate, as shown in Equation (37). To minimise the time consumption of ship manoeuvering, cost function can be written as follows:

$$\min\left(J_{\text{plan}}\right)=\min\left(\int_{s_0}^{s_f}\frac{1}{\dot{s}}ds\right) \tag{50}$$

where J_{plan} is the cost function, which is expressed as an integral of time with respect to the curve variable and $[s_0, s_f]$ represents prediction horizon in a spatial coordinate. Constraints applied at the path planning stage are defined as follows:

$$\begin{aligned}
&X_s^{'}=A_sX_s+B_su_s\\
&X_s\in\left[X_{s,\text{l}},X_{s,\text{u}}\right]\\
&u_s\in\left[u_{s,\text{l}},u_{s,\text{u}}\right]\\
&u_s^{'}\in\left[u_{s,\text{l}}^{'},u_{s,\text{u}}^{'}\right]\\
&X_s(0)=X_{s,\text{initial}}
\end{aligned} \tag{51}$$

The first constraint in Equation (51) is state space, which represents the vessel's hydrodynamics. The second constraint corresponds to the boundary condition of the states. The subscripts l and u indicate the lower and upper bounds, respectively, of the integral. The third constraint is the boundary condition of MVs. The fourth constraint is the boundary condition of the MV derivatives. The last constraint is the initial condition of the manoeuvring equation.

In the trajectory tracking stage, cost function is defined as the deviation of the tracking trajectory to the planned time-optimal trajectory, which can be written as follows:

$$\min\left(J_{\text{track}}\right)=\min\left(\int_{t_0}^{t_f}\sqrt{\left(X_{0,\text{track}}-X_{0,\text{ref}}\right)^2+\left(Y_{0,\text{track}}-Y_{0,\text{ref}}\right)^2}\,dt\right) \tag{52}$$

where X_0 and Y_0 are the positions in the earth-fixed coordinate, which is given in Equation (52) and are elements in the first two rows of the state vector. The subscript 'track' represents the tracking states and subscript 'ref' represents the planned states as a reference path. The initial and final conditions of the tracking trajectory are the same as the planned time-optimal one. Tracking trajectory is iteratively optimised by minimising its deviation to the planned time-optimal trajectory, and there are acceptable errors between planned trajectory and tracking one. Constraints applied at the trajectory tracking stage are defined as follows:

$$\begin{aligned}
&\dot{X}=A_tX_t+B_tu_t\\
&X_t\in\left[X_{t,\text{l}},X_{t,\text{u}}\right]\\
&u_t\in\left[u_{t,\text{l}},u_{t,\text{u}}\right]\\
&u_t^{'}\in\left[u_{t,\text{l}}^{'},u_{t,\text{u}}^{'}\right]\\
&X_t(0)=X_{t,\text{initial}}
\end{aligned} \tag{53}$$

in which constraints have similar meaning as the ones used in Equation (51). However, they are based on a temporal coordinate.

4.5. Extended Kalman filter estimation

An Extended Kalman filter (EKF) estimation is used in tracking simulation to reduce the influence of noise of actuators and observers. Hence, the manipulated action or observed states are not the accurate values. The EKF estimation preprocess the observed signal of updated states to make the measured data close to the real data based on the statistics theory. The EFK estimation makes the control system efficient and reliable. The EKF estimation in the temporal discrete form was shown in (Zhang et al., 2022).

5. Result analysis and discussion

Combining the methods discussed in Sections 2–4, NPMC in spatial coordinate is used to generate the time-optimal path. The controller manipulates rudder and propeller to track the planned path as a reference using temporal NMPC. EKF estimation will reduce the deviation caused by disturbances.

5.1. Description of ship manoeuvring model

The ship model used in the numerical case study is a very large crude carrier (VLCC) tanker called KVLCC2 (Stern, 2008). The detailed information of the model is available in (SIMMAN, 2008; Yasukawa and Yoshimura, 2015). Second-order wave loads for the KVLCC2 were determined from the circular motion tests reported in (Jeon et al., 2021). The principal particulars of the ship model are shown in Table 2. The maximum speed is 15.5 knots which equals to 7.974 m/s. The corresponding rotation speed of the propeller is 1.77 rotations per second (rps). The steering rate of the rudder is 1.76°/s. The radius of yaw gyration is estimated as $0.25L$, therefore, the moment of inertia in the horizontal plane is $I_{zG}=m\cdot(0.25L)^2$.

Table 3 shows the normalised hydrodynamic derivatives and coefficients of ship hull used in the numerical model. Full-scale hydrodynamic derivatives and coefficients appeared in Equation (9) are calculated based on the prime system II of SNAME and the principal particulars shown in Table 2. The propeller quantities appeared in Equations (10)–(15) are shown in Table 4. The rudder quantities appeared in Equations (16)–(24) are shown in Table 5.

The wave load acting on the ship is induced by uni-directional wave (see Table 6). The wave amplitude and wave length can be expressed by the ship length L. The wave amplitude is determined as a relatively small value compared to L, which meets the assumption of linear wave theory.

The resultant speed U is between 0 and 7.974 m/s and the incident wave length $\lambda=1.0\,L$. The hydrodynamic coefficients of wave-induced forces and moments mentioned in Equation (30) were referenced from the experimental data provided by Jeon et al. (2021), where all wave-induced forces and moments were obtained through experimental approaches for the VLCC. The spline interpolation and extrapolation are implemented to obtain the wave load coefficients at unknown ship speeds and heading angles.

5.2. Validation of ship manoeuvring model

The numerical simulations of the turning, zigzag characteristics were carried out to ensure that the nonlinear MMG model accurately assessed the maneuvering behavior of the KVLCC2. Turning circle motion and zig-zag motion of the KVLCC2's MMG model has been validated by comparing with a series of experimental tests (Kim et al., 2019) as shown in Fig. 6. The mathematical manoeuvring model predict the complicated interaction amongst the hull, propeller, rudder and wave load. When using the nonlinear MMG model adopted in this work, the agreement is reasonable for the predicted ship trajectories.

5.3. Manoeuvring and controller scenarios

ψinitial represents the initial heading angle and ψfinal is the final heading angle of the manoeuvring operation in the earth-fixed frame. In the case study section, two typical manoeuvring scenarios are proposed

Table 2
Principal particulars of the KVLCC2 tanker.

Principal particular	Symbol	Full-scale value	Unit
Ship perpendicular length	L	320.0	m
Ship breadth	B	58.0	m
Ship draft	D	20.8	m
Ship displacement	Δ	312, 600.0	m^3
Longitudinal coordinate of CoG	x_G	11.2	m
Block coefficient	C_b	0.810	–
Propeller diameter	D_p	9.86	m
Rudder span	H_R	15.80	m
Rudder area	A_R	112.5	m^2
Maximum speed	$U_{\max}$	7.974	m/s

Table 3
Normalised hydrodynamic derivatives of ship hull used in the numerical model.

Surge		Sway		Yaw	
Symbol	Value	Symbol	Value	Symbol	Value
m_x^{dl}	0.022	m_y^{dl}	0.223	J_z^{dl}	0.011
R_0^{dl}	0.022	Y_v^{dl}	−0.315	N_v^{dl}	−0.137
X_{vv}^{dl}	−0.040	Y_r^{dl}	0.083	N_r^{dl}	−0.049
X_{vr}^{dl}	0.002	Y_{vvv}^{dl}	−1.607	N_{vvv}^{dl}	−0.030
X_{rr}^{dl}	0.011	Y_{vvr}^{dl}	0.379	N_{vvr}^{dl}	−0.294
X_{vvvv}^{dl}	0.771	Y_{vrr}^{dl}	−0.391	N_{vrr}^{dl}	0.055
		Y_{rrr}^{dl}	0.008	N_{rrr}^{dl}	−0.013

Table 4
Normalised hydrodynamic derivatives of propeller used in the numerical model.

Symbol	Value	Symbol	Value
t_P	0.220	ε	1.09
C_1	2.0	κ	0.50
C_2 ($\beta_P > 0$)	1.6	k_0	0.2931
C_2 ($\beta_P < 0$)	1.1	k_1	−0.2753
w_{P0}	0.35	k_2	−0.1385

Table 5
Normalised hydrodynamic derivatives of rudder used in the numerical model.

Symbol	Value	Symbol	Value
t_R	0.387	γ_R ($\beta_R > 0$)	0.395
a_H	0.312	γ_R ($\beta_R < 0$)	0.640
x_H/L	−0.464	l_R/L	−0.710
X_R/L	−0.5	Λ	1.827

Table 6
Wave parameters used in the numerical model.

Symbol	Value
A_w/L	0.01
λ/L	1.0

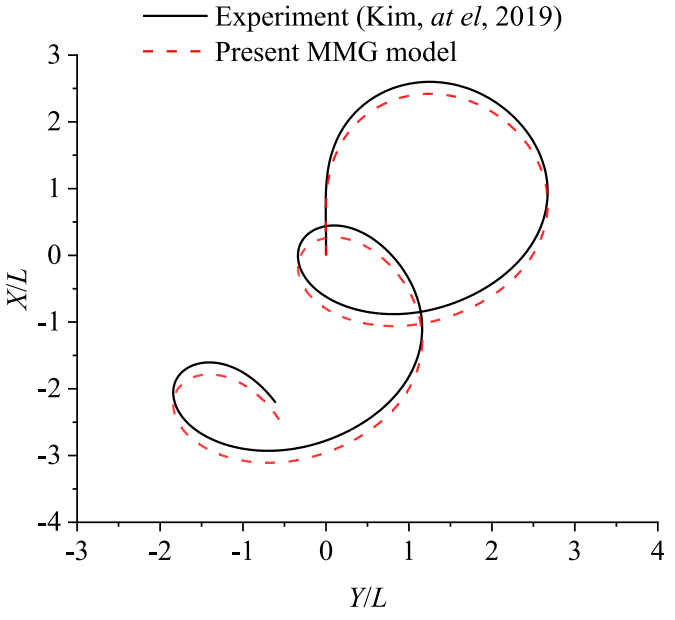

Fig. 6. Comparison of the trajectory between the experiment and MMG models for the turning maneuver in regular head waves ($\delta = 35°$, $A_w = 6.4$m, $\lambda = 0.7\,L$).

to investigate the influence of wave loads on manoeuvring operations. The initial heading angles of ship are set as 0 and 90°, while the final heading angle and the initial incident wave angle are both 0° for these two cases. The final heading angle and initial incident wave angle is 0° for both cases. The initial wave direction is normal to the x-axis. As the final heading angles are the same, here the encounter wave direction against the final position, $\gamma_{en,f}$, is used to describe the wave direction. There are only two directions shown in the case study bow and stern wave against the ship's final heading angle. The expected trajectories of the ship. The wave load varies, and at the meanwhile the encounter wave angle changes during the manoeuvring operations.

There are three different controller strategies for course planning and tracking, which can implement the wave loads:

- Strategy A exclude the wave loads in both planning and tracking process. This strategy is equivalent to the one used in calm water case. This strategy is used as a reference to evaluate the impact of wave loads on path planning and tracking.
- Strategy B only include the wave load in the course tracking process. This strategy represents that the planned path is optimised in calm water. The tracking deviation induced by wave loads will be eliminated by applying a MPC controller.
- Strategy C considers the wave load in both planning and tracking processes. In this strategy, the wave load is treated as a known quantity at the planning stage. Thus, the influence of wave loads on the propulsion and steering can be considered in the control system.

In order to investigate the impact of wave loads on manoeuvring operations, ten different scenarios were simulated. These scenarios, as detailed in Table 7, are selected to cover various controller strategies, manoeuvring conditions, and wave load conditions. The case label represents the specified scenario for simulation setup. For example, B-90-0-stern: 'B' indicates Strategy B mentioned above; '90' indicates the ship's initial heading angle is 90°; '0' indicates the final heading angle is 0°; 'stern' indicates that the wave propagates from the stern part to bow part at the final state.

5.4. Case study comparison

In this section, two sets of results will be compared: (1) planned time-optimal manoeuvring operations and planned paths; (2) tracking trajectories following the planned state variables. The former set reveals the influence of wave load on path planning and the latter set

Table 7
Manoeuvring scenarios matrix in the case study.

Case No.	Case label	Controller strategy		Manoeuvring condition		Wave load
		Planning	Tracking	ψ_0 (deg)	ψ_f (deg)	$\gamma_{en,f}$ (deg)
1	A-0-0-calm	×	×	0	0	–
2	B-0-0-bow	×	✓	0	0	180
3	C-0-0-bow	✓	✓	0	0	180
4	B-0-0-stern	×	✓	0	0	0
5	C-0-0-stern	✓	✓	0	0	0
6	A-90-0-calm	×	×	0	90	–
7	B-90-0-bow	×	✓	0	90	180
8	C-90-0-bow	✓	✓	0	90	180
9	B-90-0-stern	×	✓	0	90	0
10	C-90-0-stern	✓	✓	0	90	0

quantitively analyses the benefit of considering the wave load in the controller. There are 50 repeated simulations for each case.

Fig. 7 shows the path planning results of the time-optimal solutions. Because cases of strategies A and B use the same planning controller, the planned paths are the same. Cases of strategies A and C are shown in the figure to evaluate the wave impact on the path planning. In Fig. 7, Cases 1, 3 and 5 have similar trajectories, while Cases 6, 8 and 10 have similar trajectories. The whole manoeuvring processes can be divided into three phases: adjusting, straight, and converging phases. At the adjusting phase, the ship changes its heading direction and increases its speed. At the straight phase, the ship keeps at the highest speed and a constant heading angle. This corresponds to an optimal solution to reduce the manoeuvring time. Since the wave directions are different in cases, the trajectories at this phase start at different positions with different heading angles. It is noted that the planned trajectories under different wave loads are the same at the converging phase to ensure the ship stops at the targeted position with minimised errors of state variables.

The optimal manoeuvring time of the planning processes are listed in Table 8. Due to the random disturbance of tracking process, the values of optimal time are different for repeated simulations. Here, the optimal time is taken as the mean value of the fifty simulations repeated in each scenario. The wave impacts make the manoeuvring time significantly increase. The longest time is observed in the case C-0-0-stern. The time differences mainly occur at the adjusting stage. 10%–20% of time consumption increases significantly if the wave load exists.

The trajectory tracking results are shown in Figs. 8–11. The planned path of strategies A and B (black curves and red curves) are overlapped because the planning controller are the same. The tracking processes of strategy B can reach the target states successfully. It indicates that introducing the wave load into the controller is beneficial to the automatic manoeuvring. The failed path tracking occurs at a low probability (6 of 200 cases, 3%) for cases of strategy B. An unsuccessful case simulation is shown in Fig. 12. Disturbances of 5% is relatively large for the observation. this could be the reason of the unsuccessful tracking results. If the disturbance is restricted to a lower level, the failure rate will be closed to 0. The failure rate is 0% for all repeated 200 cases for cases of strategy C, indicating a lower safety risk if the wave loads have been considered in planning processes.

Comparing the trajectory tracking of strategies B and C (red scatters and blue scatters) in Figs. 8(a), 9(a) and 10(a), and Fig. 11(a), the tracking trajectories are following the different reference paths because of the planned references (red curves and blue curves) are generated by different types of path planning controllers. The planned time and tracking trajectories of cases of strategy C are both longer than those of cases of strategy B, which is influenced by involvement of wave load in planning optimisation.

The state variable deviation at the final position of tracking process is an important value to evaluate the performance of controller. The deviations of control strategies are shown in Table 9. The performance of the controller is evenly disturbed in three levels: high, medium, and low. The levels are represented by the green, gold and orange colours of cells, respectively. The background colours of the case labels indicate the overall performances evaluated by the six state variables. The controller of strategy C outperforms that of strategy B.

According to the result comparison, the evaluation of the two control strategies, B and C, are summarised in Table 10. Regarding to the system complexity, the strategy C is more complex than the strategy B. For an actual application, forecasting wave load by onboard devices in tracking process is easier than forecasting wave load in the planning stage. If the wave load in the planning stage is of low precision, the reliability of the planning reference path will be reduced. Regarding to the optimal manoeuvring time, the cases of strategy C have long manoeuvring time because of wave loads in the planning optimisation model. However, the involvement of wave load in the planning stage improves the robustness of the tracking process which reduces the failure probability of tracking process to zero. The selection of control strategy should be based on the

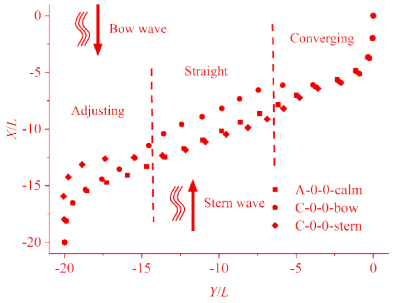

(a) Planned trajectories of cases 1, 3 and 5.

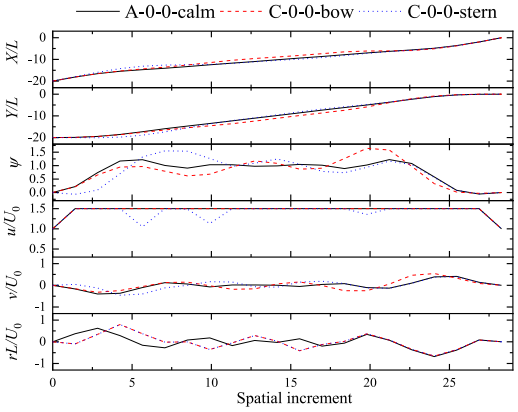

(b) State variables of cases 1, 3 and 5.

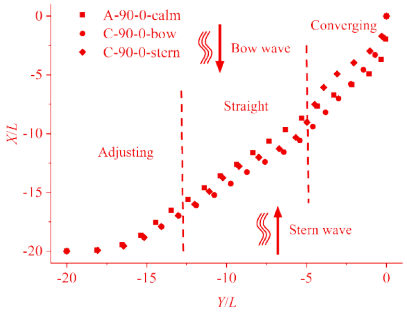

(c) Planned trajectories of cases 6, 8 and 10.

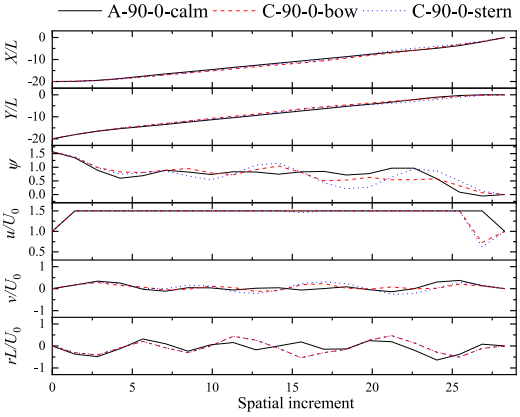

(d) State variables of cases 6, 8 and 10.

Fig. 7. Time-optimal path planning under wave loads.

Table 8
Optimal manoeuvring time of the path planning in the simulated cases.

Case label	Planned optimal manoeuvring time (s)
A-0-0-calm	837.6
C-0-0-bow	923.2
C-0-0-stern	1046.4
A-90-0-calm	824.1
C-90-0-bow	990.0
C-90-0-stern	881.2

The time-optimal state variables are interpolated with a constant time increment as introduced by Zhang et al. (2023a) is transferring the reference path form a spatial coordinate to a temporal one. In the path tracking process, 5% error is used, which indicates the measured values of observations and manipulated values of actuators are within the range from 95% to 105% of the actual values. The accuracy of the measurement is improved through the EFK estimation introduced in section 4.5.

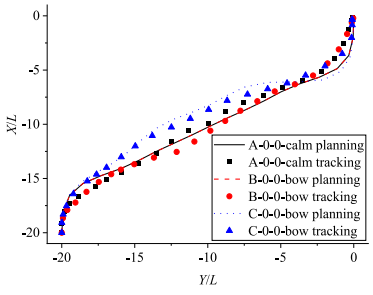

(a) Comparison of the planned and tracked trajectories.

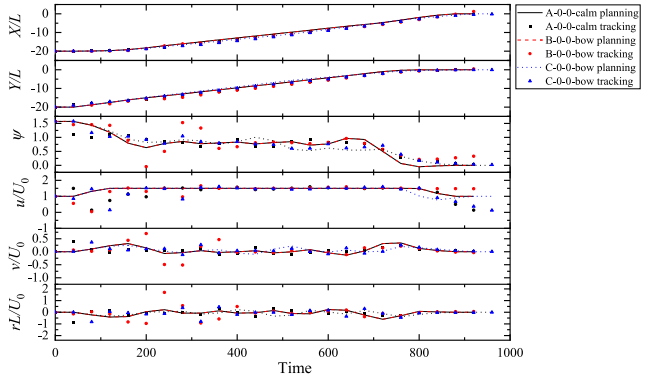

(b) Time history of state variables.

Fig. 8. Planned and tracked trajectories of cases 1, 2 and 3.

maturity of the onboard observation, actuation, and communication systems. If those systems can provide precise information to manoeuvring controller, strategy B of low system complexity can be adopted. If not, an additional wave prediction system is required to improve the operation safety. The control performance of strategy C is better than that of strategy B when comparing final deviations of state variables.

6. Conclusion

The present study focused on solving the problem of path planning and trajectory tracking for autonomous ships operating in wave conditions by means of the MPC controller. Given that autonomous ships operate in different environmental conditions, it is very important to find the optimal results for the path planning and trajectory tracking of the ship in actual seaways in order to ensure safe and efficient autonomous navigation. This paper is expected to make a valuable contribution

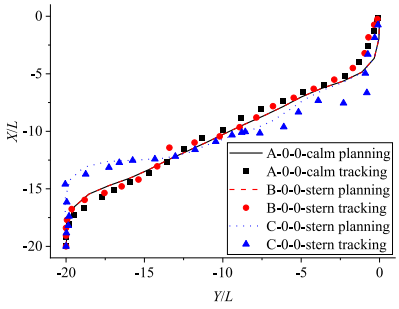

(a) Comparison of the planned and tracked trajectories.

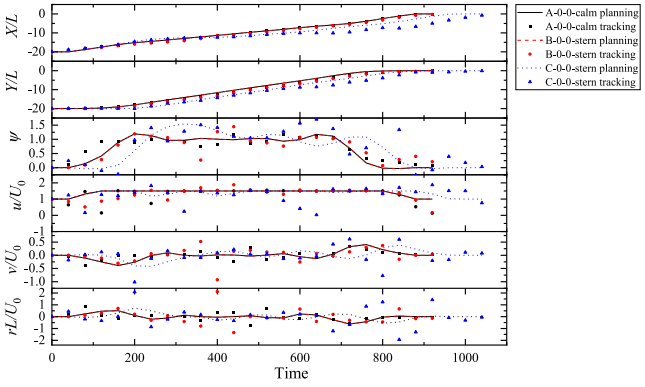

(b) Time history of state variables.

Fig. 9. Planned and tracked trajectories of cases 1, 4 and 5.

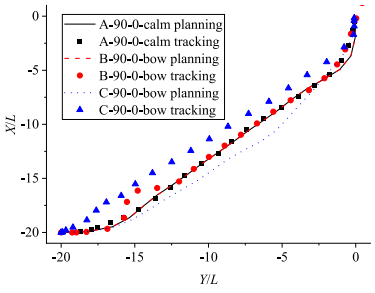

(a) Comparison of the planned and tracked trajectories.

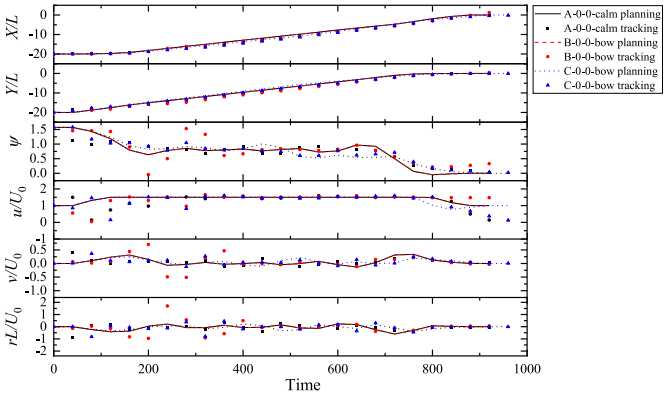

(b) Time history of state variables.

Fig. 10. Planned and tracked trajectories of cases 6, 7 and 8.

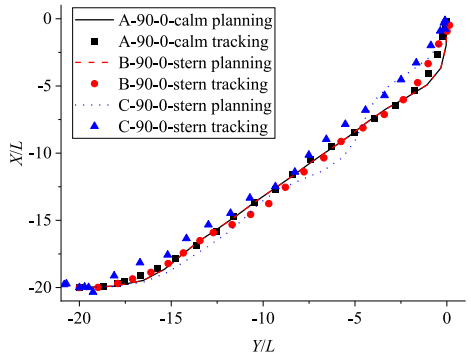

(a) Comparison of the planned and tracked trajectories.

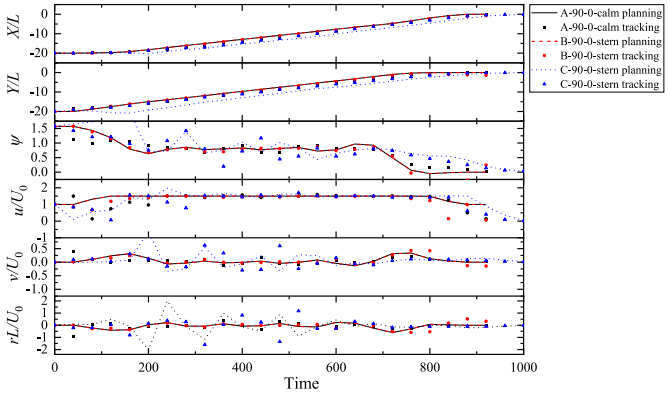

(b) Time history of state variables.

Fig. 11. Planned and tracked trajectories of cases 6, 9 and 10.

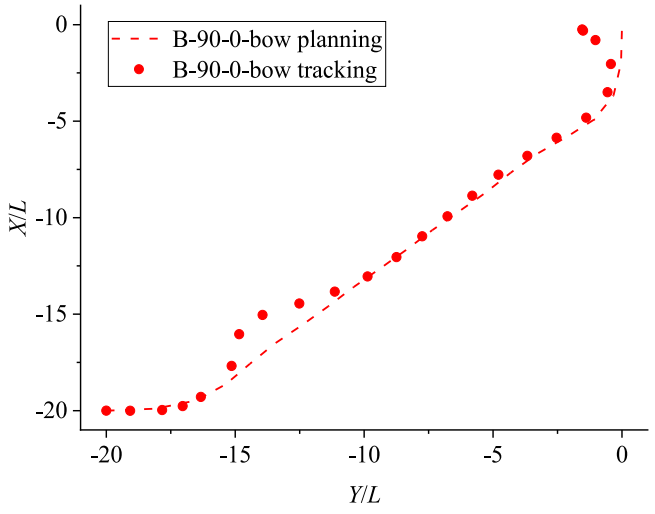

Fig. 12. Planned and tracked trajectories of a failed case simulation.

to the field of autonomous vehicles by showcasing the integration of the MPC controller with the MMG model in wave conditions.

In this study, the dynamics of a ship operating in waves were represented by the MMG model. The MPC-based algorithm is utilised to optimise manoeuvring behaviours of the ship in terms of both the path planning and trajectory tracking. In addition, spatial reformation is introduced to realise time-optimal optimisation. The wave loads are simplified as constant 2-order force and moment neglecting sinusoidal

Table 9
State variable deviations at the final positions of tracking processes.

Case No.	Case label	$\lvert X/L\rvert$	$\lvert Y/L\rvert$	$\lvert\psi\rvert$	$\lvert uL/U_0\rvert$	$\lvert vL/U_0\rvert$	$\lvert rL/U_0\rvert$
1	A-0-0-calm	0.15	0.07	0.06	0.13	0.03	0.04
2	B-0-0-bow	0.22	0.03	0.06	0.18	0.04	0.05
3	C-0-0-bow	0.35	0.10	0.00	0.25	0.00	0.02
4	B-0-0-stern	0.25	0.13	0.21	0.17	0.05	0.13
5	C-0-0-stern	0.36	0.10	0.03	0.26	0.08	0.05
6	A-90-0-calm	0.17	0.03	0.04	0.14	0.02	0.03
7	B-90-0-bow	0.35	0.06	0.10	0.30	0.06	0.10
8	C-90-0-bow	0.48	0.15	0.02	0.40	0.07	0.10
9	B-90-0-stern	0.64	0.38	0.24	0.06	0.15	0.32
10	C-90-0-stern	0.10	0.05	0.04	0.02	0.01	0.02

Table 10
Optimal time of the path planning in the simulated manoeuvring cases.

Evaluation	Strategy B	Strategy C
System complexity	Low	High
Planning time	= calm water	> calm water
Tracking failure	3%	0%

load components. The wave load is determined by encounter wave angle, ship speed and wave length. Ten cases are illustrated combining different control strategies, ship's initial positions and wave conditions to quantitatively analysis the impact of wave loads. The main findings of this study can be summarised as follows:

(1) The involvement of wave load can increase the expected manoeuvring time of ship in both of strategies B and C, and the planning controller generate different paths compared to the paths of calm water when introducing wave loads in strategy C.
(2) The whole manoeuvring operation can be divided into three phases: adjusting, paralleling, and converging phases. The phenomenon is determined by the time optimisation algorithm.
(3) Two control strategies are evaluated for ship manoeuvring control system. Strategy B have low system complexity whilst low overall performance. Strategy C is more reliable and better performance. However, the wave prediction in planning process is an additional burden for ship controller.

The present methodology is designed for path planning and tracking of two waypoints. Am MPC-based control algorithm for multi-waypoint paths are required in the further research. Only regular wave load is considered in the present study, irregular wave load will be a challenging and breakthrough for path planning and tracking.

CRediT authorship contribution statement

Ming Zhang: Writing – original draft, Software, Methodology, Formal analysis. **Daejeong Kim:** Writing – review & editing, Software. **Tahsin Tezdogan:** Writing – review & editing. **Zhi-Ming Yuan:** Writing – review & editing, Supervision, Formal analysis.

Declaration of competing interest

The authors declare the following financial interests/personal relationships which may be considered as potential competing interests: Ming Zhang reports financial support was provided by National Natural Science Foundation of China.

Data availability

No data was used for the research described in the article.

References

Fossen, T.I., 2011. Handbook of Marine Craft Hydrodynamics and Motion Control. John Wiley & Sons.

Fujii, H., Tuda, T., 1961. Experimental researches on rudder performance.(2). J. Zosen Kiokai 1961 (110), 31–42.

Helling, S., Roduner, C., Meurer, T., 2021. On the Dual Implementation of Collision-Avoidance Constraints in Path-Following MPC for Underactuated Surface Vessels, 2021 American Control Conference. ACC). IEEE, pp. 3366–3371.

Huang, Y., Chen, L., Chen, P., Negenborn, R.R., Van Gelder, P., 2020. Ship collision avoidance methods: state-of-the-art. Saf. Sci. 121, 451–473.

Huang, Y., Ding, H., Zhang, Y., Wang, H., Cao, D., Xu, N., Hu, C., 2019. A motion planning and tracking framework for autonomous vehicles based on artificial potential field elaborated resistance network approach. IEEE Trans. Ind. Electron. 67 (2), 1376–1386.

Im, N., 2012. A study on ship automatic berthing with assistance of auxiliary devices. Int. J. Nav. Archit. Ocean Eng. 4 (3), 199–210.

Jeon, M., Mai, T.L., Yoon, H.K., Kim, D.J., 2021. Estimation of wave-induced steady force using system identification, model tests, and numerical approach. Ocean. Eng. 233, 109207.

Kim, D.J., Yun, K., Park, J.-Y., Yeo, D.J., Kim, Y.G., 2019. Experimental investigation on turning characteristics of KVLCC2 tanker in regular waves. Ocean. Eng. 175, 197–206.

Kim, H., Kim, S.-H., Jeon, M., Kim, J., Song, S., Paik, K.-J., 2017. A study on path optimization method of an unmanned surface vehicle under environmental loads using genetic algorithm. Ocean. Eng. 142, 616–624.

Kouvaritakis, B., Cannon, M., 2016. Model Predictive Control, vol. 38. Springer International Publishing, Switzerland.

Liu, Y., Bucknall, R., Zhang, X., 2017. The fast marching method based intelligent navigation of an unmanned surface vehicle. Ocean. Eng. 142, 363–376.

Maki, A., Sakamoto, N., Akimoto, Y., Nishikawa, H., Umeda, N., 2020. Application of optimal control theory based on the evolution strategy (CMA-ES) to automatic berthing. J. Mar. Sci. Technol. 25 (1), 221–233.

MathWorks, 2019. Compute Gradients for Custom Training Loops Using Automatic Differentiation. https://uk.mathworks.com/help/deeplearning/ref/dlarray.dlgradient.html#responsive_offcanvas.

Matsumoto, K., Suemitsu, K., 1980. The prediction of manoeuvring performances by captive model tests. J. Kansai Soc. Nav. Archit. Jpn. 176, 11–22.

Mizuno, N., Kuroda, M., Okazaki, T., Ohtsu, K., 2004. Minimum time ship maneuvering using neural network and nonlinear model predictive compensator. IFAC Proc. Vol. 37 (10), 297–302.

Oh, S.-R., Sun, J., 2010. Path following of underactuated marine surface vessels using line-of-sight based model predictive control. Ocean. Eng. 37 (2–3), 289–295.

Ohtsu, K., Shoji, K., Okazaki, T., 1996. Minimum-time maneuvering of a ship, with wind disturbances. Control Eng. Pract. 4 (3), 385–392.

Okazaki, T., Ohtsu, K., 2008. A study on ship berthing support system-Minimum time berthing control. In: 2008 IEEE International Conference on Systems, Man and Cybernetics. IEEE, pp. 1522–1527.

Pavlov, A., Nordahl, H., Breivik, M., 2009. MPC-based optimal path following for underactuated vessels. IFAC Proc. Vol. 42 (18), 340–345.

Salvesen, N., 1974. Second-order steady state forces and moments on surface ships in oblique regular waves. In: Proceedings of the International Symposium on Dynamics of Marine Vehicles and Structures in Waves. University College, London, 1974.

Simman, 2008. MOERI Tanker KVLCC2.

Stern, F., 2008. Part B: Benchmark Test Cases, Preprints of Workshop Proceedings, Workshop on Verification and Validation of Ship Manoeuvring Simulation Methods. SIMMAN, pp. B3–B14, 2008.

Verschueren, R., De Bruyne, S., Zanon, M., Frasch, J.V., Diehl, M., 2014. Towards Time-Optimal Race Car Driving Using Nonlinear MPC in Real-Time, 53rd IEEE Conference on Decision and Control. IEEE, pp. 2505–2510.

Wahl, A., Gilles, E.-D., 1998. Track-keeping on waterways using model predictive control. IFAC Proc. Vol. 31 (30), 149–154.

Wang, X., Yao, X., Zhang, L., 2020. Path planning under constraints and path following control of autonomous underwater vehicle with dynamical uncertainties and wave disturbances. J. Intell. Rob. Syst. 1–18.

Yasukawa, H., Yoshimura, Y., 2015. Introduction of MMG standard method for ship maneuvering predictions. J. Mar. Sci. Technol. 20, 37–52.

Zhang, J., Sun, T., Liu, Z., 2017. Robust model predictive control for path-following of underactuated surface vessels with roll constraints. Ocean. Eng. 143, 125–132.

Zhang, M., Hao, S., Wu, D., Chen, M.-L., Yuan, Z.-M., 2022. Time-optimal obstacle avoidance of autonomous ship based on nonlinear model predictive control. Ocean. Eng. 266, 112591.

Zhang, M., Yu, S.-R., Chung, K.S., Chen, M.-L., Yuan, Z.-M., 2023a. Time-optimal path planning and tracking based on nonlinear model predictive control and its application on automatic berthing. Ocean. Eng. 286, 115228.

Zhang, M., Yuan, Z.-M., Tao, L., Shi, W., 2023b. A NOVEL CONCEPTUAL DESIGN OF MODULARISED OFFSHORE GREEN HYDROGEN SYSTEM. OMAE2023, Melbourne, Australia.